We are IntechOpen,
the world's leading publisher of
Open Access books
Built by scientists, for scientists

6,900
Open access books available

185,000
International authors and editors

200M
Downloads

154
Countries delivered to

Our authors are among the

TOP 1%
most cited scientists

12.2%
Contributors from top 500 universities

BOOK CITATION INDEX
CLARIVATE ANALYTICS
INDEXED

WEB OF SCIENCE™

Selection of our books indexed in the Book Citation Index
in Web of Science™ Core Collection (BKCI)

Interested in publishing with us?
Contact book.department@intechopen.com

Numbers displayed above are based on latest data collected.
For more information visit www.intechopen.com

Chapter

Effect of Textures and Microstructures on the Occurrence of Delamination during and after Fracture Toughness Tests of API X80 Steel Plates

Fabio Faria Conde, Haroldo Cavalcanti Pinto, Mohammad Masoumi and Julian Arnaldo Avila

Abstract

The API 5 L X80 is a high strength microalloyed steel, widely used in the gas and oil industry to fabricate pipelines. This steel presents a combination of elevated strength and toughness. In the present investigation, the microstructural features, fracture toughness and delamination occurrence of two X80 grade steel plates with different processing routes and chemical composition were studied. The first steel depicted a homogenous bainitic matrix and the second steel exhibited a banded microstructure composed of elongated ferrite grains, with macrosegregation in the mid-plane of the plates. Fracture toughness tests were conducted for both steels on 7-mm and 15-mm thick samples. The orientation distribution functions analysis revealed crystallographic intensity distribution of the austenite to ferrite transformation texture, especially the alpha-fiber (< 011 > ‖ rolling direction) which explained the anisotropy and delamination occurrences. Both processed plates of steel presented the alpha-fiber due to hot-rolling of plates. Delaminations occurrences were further investigated and attributed to a strong {100} <011> orientation presence despite microstructure homogeneity. A schematic model was proposed, showing the source of delamination and the reason for the lowest toughness for 45° to the rolling direction.

Keywords: crystallographic texture, fracture toughness, mechanical strength, microstructure characterization, TMCP, X80 plates of steel, pipeline steel

1. Introduction

The efficiency of pipeline transport systems, widely employed in the oil and gas industries, depends, to a significant extent, on increasing diameters and working pressures while reducing the wall thickness to lower the cost per transport unit [1, 2]. In this context, pipeline steels have been continuously developed toward increased strength, toughness, and formability, as well as maintaining low carbon composition to ensure adequate weldability [1, 2]. In order to achieve these goals, pipeline steels, such as API 5 L X80, X100, and X120, rely upon alloy design and

Thermo-Mechanically Controlled Processing (TMCP) to produce grain refinement by controlled deformation of austenite during rolling [3, 4]. In general, rolling of TMCP steel plates are carried out in two stages: first, rough rolling is performed in the temperature range of austenite recrystallization while alloying elements are in solution (normally above 1100°C); then, at lower temperatures (typically below 1000°C, sometimes in the intercritical range) finish rolling passes are executed, cold-working the matrix [4–6]. At these lower temperatures, the presence of precipitated carbides inhibit grain growth, and fine austenite grains, substructure, and dislocations assist the formation of a refined ferritic or bainitic structure, depending on the cooling conditions [4, 7]. Because of the low-temperature rolling, diffusional phenomena are limited, and the deformed microstructure carries strong crystallographic textures, which lead to anisotropy and possibly a decrease of mechanical properties [4, 5, 8]. As such, numerous investigations have been performed recently to understand texture formation in TMCP steels and its correlation with mechanical properties, especially impact toughness behavior (Charpy tests) [5, 6, 8–10].

Fracture toughness and how crack propagation occurs in steels, depend on their chemical composition [4, 5, 11–13], resultant microstructures [4, 5, 10–12, 14], inclusions [4, 5, 11, 12], grain morphology, e.g., pancaked or elongated [4, 12], crystallographic textures [4, 5, 10–14] and residual stresses produced after the TMCP process [15]. Moreover, many studies in the literature point out the crystallographic orientation as the major cause of delamination, i.e., the presence of 001 plane more specifically [5, 8, 11, 15–18]. Most of the literature presents impact toughness results from Charpy tests. Charpy tests are recommended for qualitative estimation of toughness, with samples that can be machined with low-cost, tests are conducted rapidly, and results are easily processed [19]. For accurate measurements of toughness, crack-tip opening displacement (CTOD) tests are recommended [20]. Also, the crack-tip constraint of Charpy samples changes due to the dynamic loading [21], however, a pipeline under operative conditions do not suffer impact loads, but rather a quasi-static evolution of pressure and internal forces. CTOD tests, with samples designed to guarantee a constant crack-tip triaxiality [21], which represents a crack propagation on opening mode I in quasi-static conditions, has not been well documented in the literature related to the fracture toughness measurement of pipelines.

Delamination is a brittle fracture behavior reported in TMCP steels [9, 17, 22–25], which occurs at the weakest interface, usually near the crack tip. There are two types of delamination based on its geometry: (i) crack divider and (ii) crack arrester. The divider branches the crack into a series of cracks traveling a narrower path [22, 23]. The arrester delamination does not result in crack branching, maintaining the same width of propagation. However, it reallocates the crack at a region with no plastic zone ahead of the crack, triggering the re-initiation of the crack under conditions of nearly uniaxial tension, resulting in high absorption of energy [22, 23]. There are several reports of delaminations of both types in Charpy tests in the literature [9, 17, 23–25] and few reports of delaminations during CTOD tests in the literature [8].

Zong et al. studied the influence of crystallographic orientation upon impact toughness through Charpy impact tests on an API X100 steel [17]. The influence of microstructure on the toughness results was excluded by using the same steel plate. The influence of crystallography orientation was assessed by milling out samples from the different orientation, 0, 30, 45, 60 and 90° tilted from rolling direction. The best condition was found at 0° and then at 90° [17], where the fracture orientation factor, a factor used to characterize the anisotropy of the fracture strength based on <100>, presented lower values compared to 45° to RD, the direction in

which maximum fracture orientation factor was obtained. Bakshi et al. [5] studied the influence of the TMCP, microstructure and crystallography on an X70 also varying the orientation of the machined samples for Charpy impact tests. As many cited works, Bakshi et al. [5] also reported that the presence of 001 plane induces delamination.

Pyshmintsev et al. [26] suggested that the clustering of (001) cleavage plane parallel to the crack plane does not lead to delamination and splitting phenomena, but that microstructure plays the major role. It was reported that prior austenite grain boundary with cube rotation texture lying parallel to crack plane propagation causes severe splitting [26]. Another study [27], reported that the anisotropy in Charpy tests results could be correlated to factors as the spatial grain distribution, grain shape, and the distribution of the phases and microconstituents, mainly the hardening ones. Kimura et al. reported that grain size was the main key to control yield strength and delamination. By applying a TMCP, ultra-fined grain was obtained, increasing the yield strength and triggering delaminations of crack-arrest type, increasing toughness as well [23].

In this work, we aim to determine the causes of the occurrence of delamination occurring during and after fracture toughness tests. The present investigation was conducted using crystallographic textures, microstructures analysis by light optical microscopy (LOM), scanning electron microscopy (SEM) coupled with energy-dispersive x-ray spectroscopy (EDS), electron back-scattered diffraction (EBSD), X-ray diffraction (XRD), and mechanical assessment with tensile tests and fracture toughness test, specifically crack-tip opening displacement (CTOD) tests, in two steel plates of X80 fabricated by TMCP. In addition, a complete fractographic analysis was conducted. The first steel was air-cooled after the last rolling pass in the intercritical region, referred in the text as the AIR-steel. It presented a banded microstructure and segregation in the mid-thickness of the plate, with elongated manganese sulfide particles and pearlite colonies. The second steel, hereafter designated as ACC-steel, underwent accelerated-cooling after finish rolling and exhibited a bainitic matrix with equiaxed bainite packages.

2. Materials and methods

Two plates of X80 grade TMCP steels, produced elsewhere using different cooling conditions, air-cooling (AIR-steel) and accelerated-cooling (ACC-steel) after finish rolling in the intercritical range, were used in the present study. The chemical composition of both steel plates is shown in **Table 1**, which is in good agreement with the ISO 3183 standard [28] requirements.

The fracture toughness assessment was conducted using CTOD tests, with experimental testing according to the ASTM 1820-13 standard [29]. Rectangular

Steel	C	Mn	V	Nb	Ti	Si	Mo	Ni	P*	S*
ISO 3183 standard [28]	0.18	1.9	*	*	*	0.45	0.5	1	250	150
ACC-steel	0.05	1.73	0.01	0.04	0.01	0.26	0.18	0.25	90	4
AIR-steel	0.08	2.07	0.04	0.07	0.01	0.22	0.18	0.01	50	22

*ISO 3183 standard [28] was used for comparisons purpose (*ppm).*

Table 1.
Chemical composition of the ACC-steel and AIR steel (wt.%).

(Bx2B) single edge bending notched samples with different thicknesses (B) of 7 and 15 mm were assessed. First, the 7-mm-thick samples were tested at 25°C to analyze the effect of the crack propagation direction in fracture toughness; therefore notches were located through the transverse (L-T) and longitudinal (T-L) direction (more details about crack orientation the ASTM E1823 standard [30]). After that, the direction of best fracture toughness result of the 7-mm-thick samples in each steel was chosen to conduct tests in thicker plates (15 mm), to increase the constraint of the crack-tip and assess the effect of temperature. 15-mm-thick samples were assessed at 0, −20 and −40°C, using the L-T direction in the AIR-steel and T-L direction in the ACC-steel. Notice that ACC-steel CTOD results were previously reported by Avila et al. [31]. Side grooves were machined on 15-mm-thick samples after pre-cracking to increase triaxiality state at the crack-tip, with straight crack-tip fronts during the CTOD tests.

Tensile tests were conducted in cylindrical samples with a diameter of 6 mm in the reduced area, following ASTM E8 standard [32]. Tensile samples were machined in rolling and transverse directions. The tensile tests were also conducted at temperatures 25, 0, −20 and −40°C.

X-ray Diffraction (XRD) was conducted to assess crystallographic texture along the normal and transverse directions (ND-TD). CuKα radiation with wavelength $\lambda = 1.54059$ Å, a continuous scanning speed of 0.14°/min, 0.02° per step and 2θ range of 40 to 100° were used during the X-ray measuring. Experimental pole figures were determined by varying azimuthal angle phi (φ) 0 to 360° in 3° steps and tilting angle chi (χ) from 0 to 87° in 3° steps. Orientation distribution functions (ODFs) were obtained from independent measurements of the (110), (200) and (211) planes.

For metallographic purposes, samples were ground from 100-grit up to 1200-grit SiC paper. Polishing was performed with diamond pastes of 3 and 1 μm and final polishing was performed in a silica suspension with 0.06 μm particle size.

Microstructural characterization was carried out on all three planes: rolling, transverse, and normal, where the rolling plane is perpendicular to the rolling direction (RD), likewise the transverse plane to TD and normal plane to ND. LOM, SEM coupled with an EDS and EBSD detectors, and Vickers hardness measurements were performed. The EBSD measurements were conducted on non-etched samples and two different magnifications were used. Areas of 1500x1300 μm^2 with a step size of 2.5 μm and 75×65 μm^2 with step sizes of 0.1 μm were used. Misorientation above 15° was used to considered grain boundaries. Then the effective grain size was determined using the area method. Grain size measured by the linear intercept technique, was carried out on LOM images. Samples were etched with 2% Nital.

3. Results

3.1 Microstructure

Figure 1a–c shows the microstructure of both steel plates. Microstructural misorientation cubes in **Figure 1d**, **e** present the microstructure morphology and distribution near the mid-thickness. The fine secondary phases and constituents (SP) presence between ferrite grains in steels depends on the alloying elements and their effect on the transformation kinetics during cooling [33]. The air-cooling after the finishing rolling pass provides enough time at elevated temperature, enabling diffusion and resulting in a variety of incomplete transformations and microconstituents classified into martensite-austenite (M-A), degenerated pearlite (DP), bainite and martensite [33–35]. The AIR-steel exhibited, in **Figure 1a**, **b**, a banded

microstructure composed by polygonal ferrite, some quasi-polygonal ferrite, pan-cake grains evidencing a finishing rolling pass at an intercritical temperature, with the formation of banding of fine phases and constituents. A macrosegregation band in the mid-plane induced by solidification is visible on the transverse plane.

The ACC-steel presented a homogenous microstructure, as shown in **Figure 1c**, **d**, over the transverse and rolling planes composed by granular bainite, with more equiaxed shape, some elongated grains, and SP. Grain size measurements using EBSD data and conventional optical procedure showed similar values, around 1.2 μm, as shown in **Table 2**. However, based on the standard deviation, the grain sizes can be considered similar in both steel plates.

The ACC-steel presented a chemical composition with lower alloying elements content than AIR-steel, resulting in less MA and microconstituents dispersed on a bainitic matrix. The ACC-steel depicted a fine ferrite and bainite matrix with dispersed SP. In addition, the accelerated-cooling suppressed diffusion and favored the formation of bainite products, as packets of bainite and granular bainite [33, 36]. According to Bhadeshia et al. [37], bainite formation takes place first by the growth of one single crystal and formation of clusters, known as packet sheaves, by the cooperative growth of other crystals, with low misorientation angles between the sub-units. As ACC steel had a bainitic microstructure, it presented a higher content
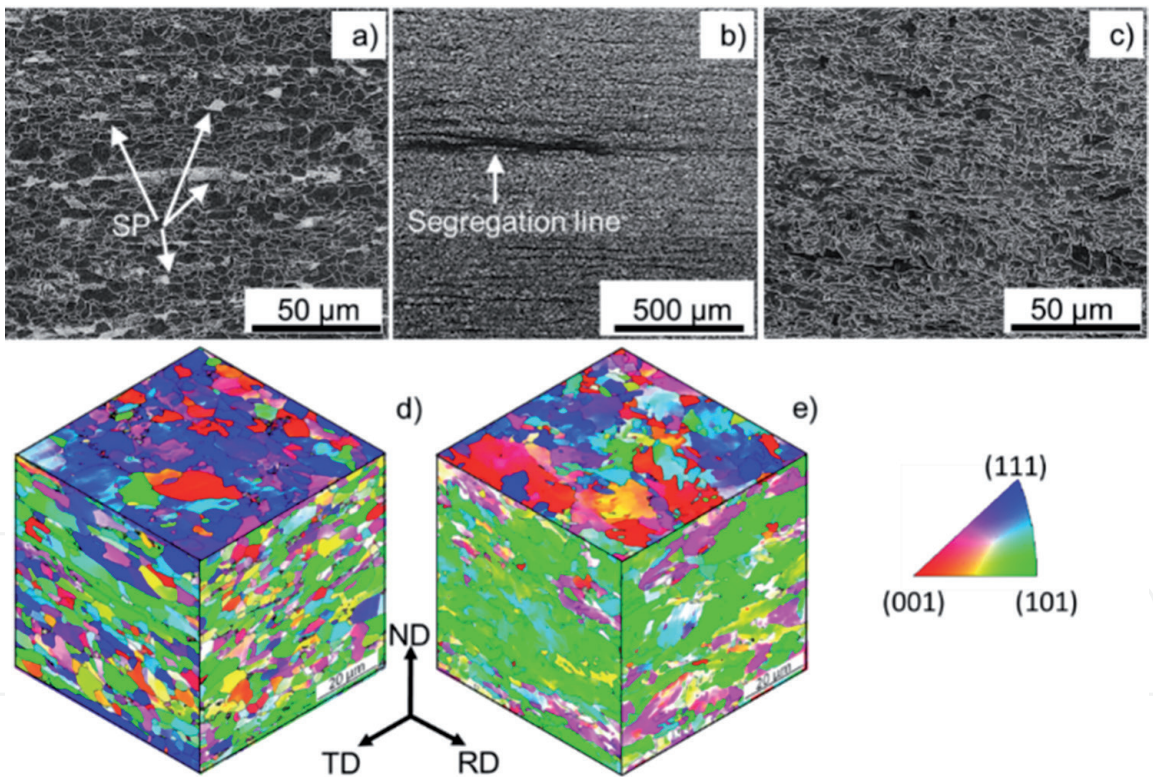
Figure 1.
SEM micrographs of the rolling plane of the plates: (a, b) AIR-steel presenting segregation and secondary phases (SP), (c) ACC-steel showing a homogeneous microstructure. Misorientation angle distribution cubes of (d) AIR-steel and (e) ACC-steel. Grain boundary misorientation >10°.

Steel	EBSD	Optical measurements
AIR	1.2 ± 0.05	1.0 ± 0.03
ACC	1.4 ± 0.05	1.2 ± 0.03

Measurements in μm.

Table 2.
Grain size values of the studied steels.

of low angle misorientation, between 5 and 15°, than the AIR-steel. The ACC steel presented similar morphology on both planes, rolling and transverse, as shown in **Figure 1e** since the accelerated-cooling resulted in a larger ferrite//bainite nucleation rate. Furthermore, the microstructure did not present elongated ferrite, evidencing a finishing rolling pass at a full austenitization temperature.

SP were observed in both plates of steel distributed around the ferritic matrix, as shown in **Figure 2a**, **b**. However, the AIR-steel presented a higher number of constituents within the light contrast bands, such as SP bands depicted in **Figure 2a** and zoomed-in in **Figure 2b**. The SP was composed of elongated and massive shapes of DP and M-A, and manganese sulfide (MnS), as detailed in **Figure 3**.

EDS analysis conducted at the mid-thickness on a specific region confirms the presence of MnS in the AIR-steel. These elongated MnS particles also depict silicon and titanium presence, as shown in **Figure 4**. ACC-steel did not show segregation in the mid-thickness.
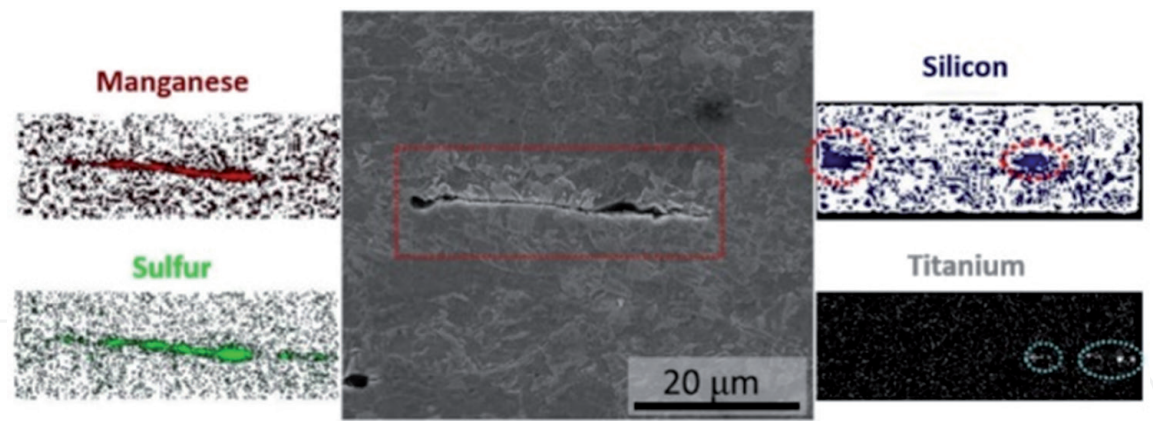
3.2 Hardness

The average hardness of the steel plates in the through-thickness direction was 238 ± 4 HV for the ACC-steel and 220 ± 4 HV for AIR-steel. There was no significant difference in hardness between rolling and transverse planes of each plate of steel considered separately, as shown in the hardness profiles presented in **Figure 4**.

3.3 Crystallographic texture

ODFs were constructed from the XRD and EBSD data and plotted in colored intensities diagrams using Bunge notation in Euler space, as depicted in **Figure 5**. The crystallographic representation for rolled steels is composed of a plane {hkl} which lies parallel to the normal plane and a direction <uvw>, which is parallel to the rolling direction [38] as schematically shown in **Figure 5e**. The reference system is based on RD, TD and ND, where their related planes are rolling, transversal and normal planes which lies perpendicular to their respective directions. The development of texture produced during hot-rolling at full austenitic region causes
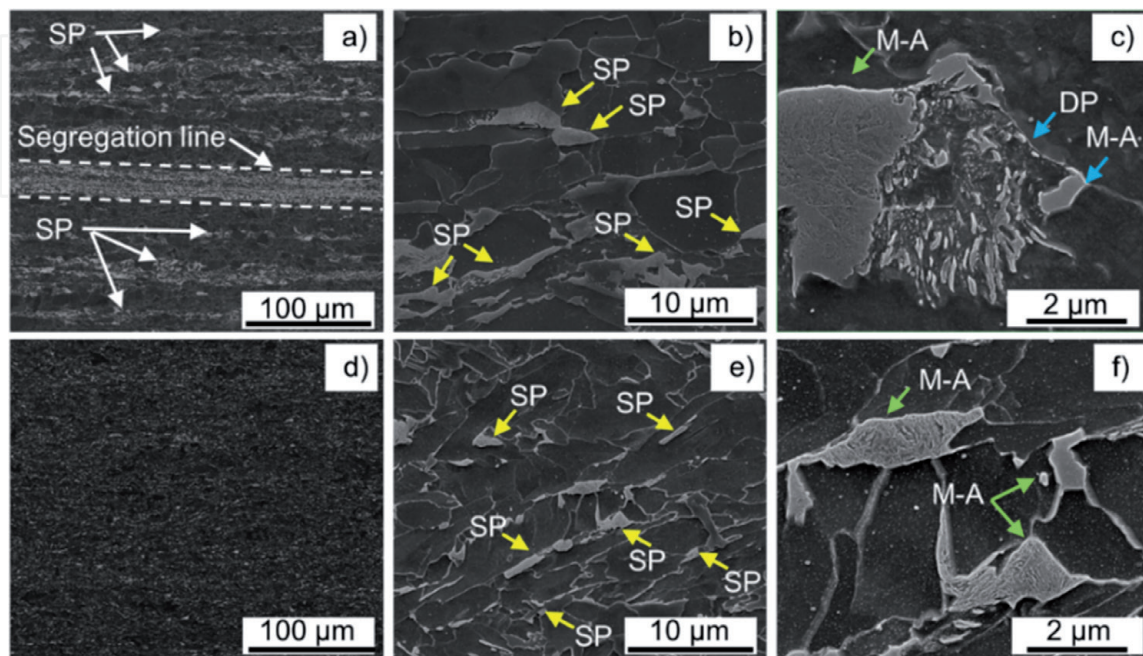
Figure 2.
*SEM micrographs of (a)–(c) AIR-steel and (d)–(f) ACC-steel.*

Figure 3.
EDS analysis of MnS elongated particles in the AIR-steel.
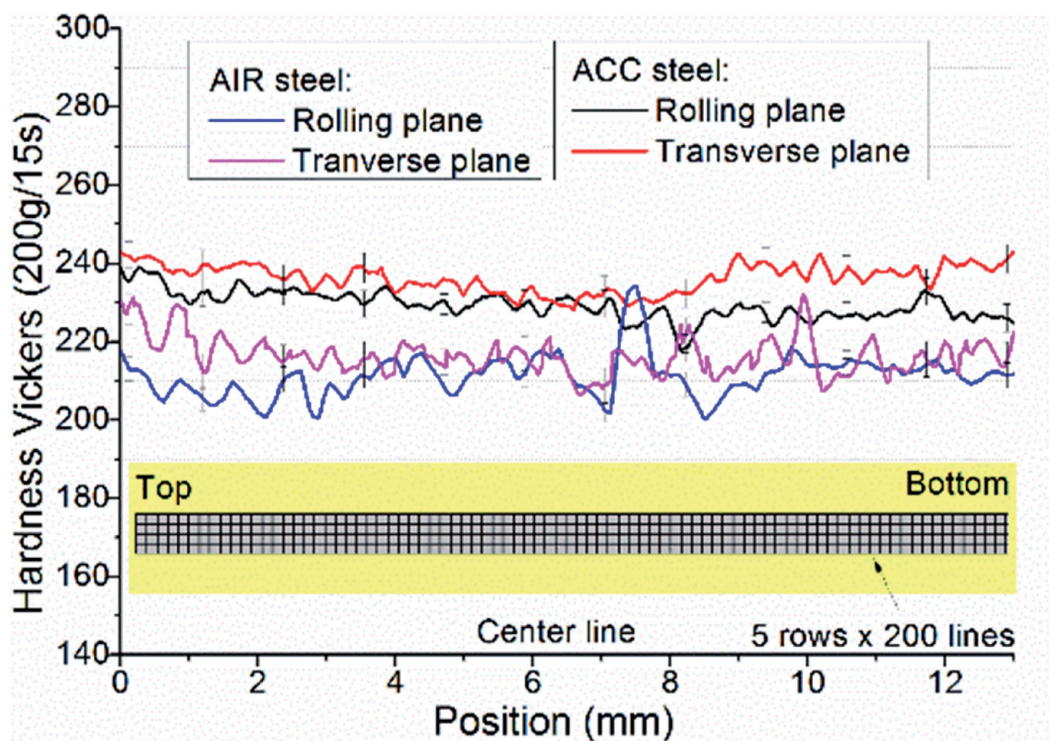
Figure 4.
Through-thickness hardness profiles in the rolling and transverse planes of the steel of ACC-steel and AIR-steel.

strong alpha-fiber development, which consists of {001} <110> to {110} <110> in
$\phi2 = 45°$, $\phi1 = 0°$, $\phi = 0–90°$ [38]. It is a rotation on the {110} direction axis, being a
fiber parallel to RD. As temperature decreases and cold-work increases, there is an
increase of gamma-fiber, which consists of {111} <110> to {111} <112> in $\phi2 = 45°$,
$\phi1 = 0–90°$, $\phi = 55°$ [38]. It is a rotation around the {111} plane, i.e., around the
perpendicular direction of the plane, which is [111], being a parallel fiber to ND. In
Figure 5a–d are retrieved the ODFs colored intensities, showing the presence of
alpha-fiber and gamma-fiber. Both steels presented low gamma-fiber intensity
compared to alpha-fiber. Comparing crystallographic textures in both steels,
AIR-steel presented higher alpha-fiber and higher crystallographic intensity in
XRD and EBSD measurements than ACC-steel as depicted in **Figure 5a–f**. Another
component that plays an important role is the cube side lattice {100} since it is the
cleavage plane on body-centered cubic (BCC) steels. The family plane {100} is likely
to have a relationship to the occurrence of delaminations, as is described further in
the present work.
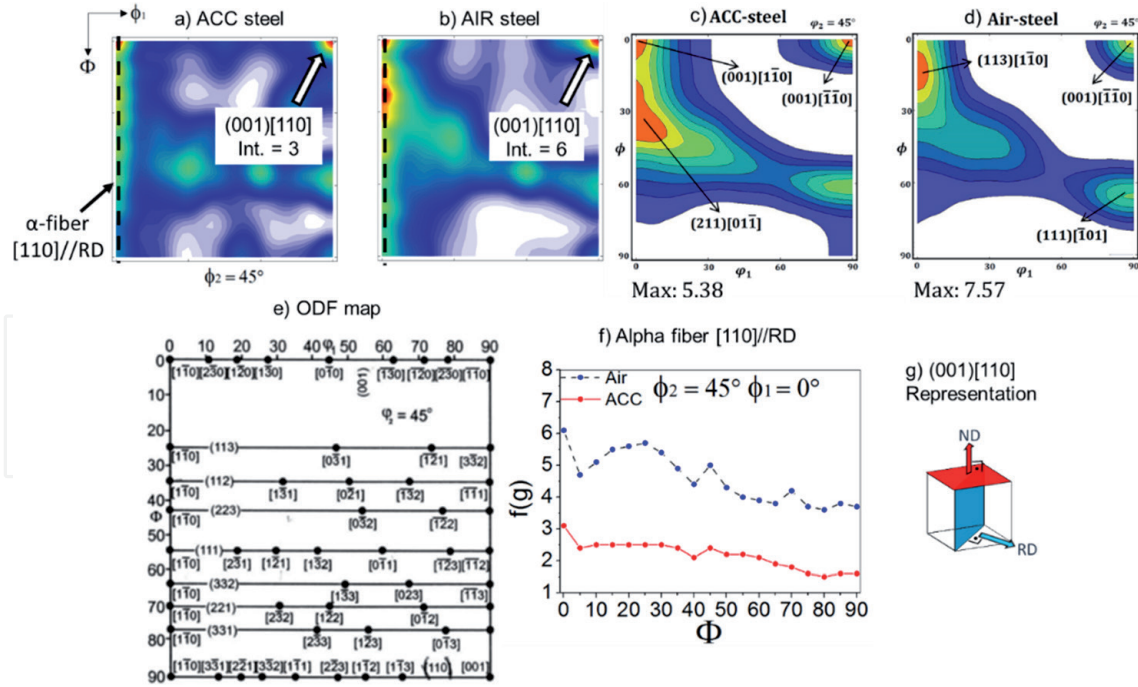
Figure 5.
ODF plots at φ2 = 45° highlighting alpha-fiber presence, location and high intensity of (001)[110]: (a, b) XRD ODF analysis: (a) ACC-steel, (b) AIR-steel; (c, d) EBSD ODF analysis: (c) ACC-steel, (d) AIR-steel;(e) ODF map [39], (f) quantification of alpha-fiber intensity by XRD, showing higher values for AIR-steel, and (g) schematic representation of crystallographic (001) planes perpendicular to ND and [110] direction parallel to RD.

The crystallographic orientation distribution from EBSD analyses was performed to compare and validate that of XRD. The EBSD analyses were carried on rolling plane of both investigated samples out at areas of 1500×1300 μm^2 with a step size of 2.5 μm containing about 1500 grains. Their related ODFs were calculated using the statistical method of kernel density estimation and presented in **Figure 5**. The results obtained by EBSD are similar to previous ODF results calculated by XRD. A certain difference between these methods could be attributed with a high statistical symmetry at each pole figure (XRD) and local grain orientation (EBSD). Overall texture intensity of AIR-steel was higher rather than ACC-steel due to the formation of {110}//RD grains accompanied by banded microstructure. Suikkanen et al. [40] characterized a {110} plane of the carbide-free bainitic ferrite similar to the martensitic transformation originated from close-packed {111} austenite plane because of the accommodation of transformation strains, enhancing the bainitic transformation. The formation of (211)[011] component could be explained by Shackleton and Kelly works which reported that the habit plane of cementite in lower bainitic ferrite is corresponding to {001}$_\theta$//{211}$_\alpha$ [41]. In other words, the proeutectoid cementite habit induced large shear deformations because of stereological effects to form a displacive bainite structure.

In order to investigate the role of local crystal orientations and boundary types, detailed EBSD measurements were carried out in rolling transversal planes of both AIR and ACC steels. Orientation image (OI) map, Kernel average misorientation (KAM) map, grain boundary (GB) map, Taylor factor (TF) maps, and normal direction pole figure (IPF) maps of each measurement were presented in **Figure 6** for AIR-steel and **Figure 7** for ACC-steel.

The orientation data collected with EBSD displayed by OIM or Euler colored maps, provides a basic presentation of the measured orientation. Grain boundaries are considered as crystal lattice defects, which can be identified by the point-to-point misorientation between neighboring data points, **Figures 6a and 7a**. Grain
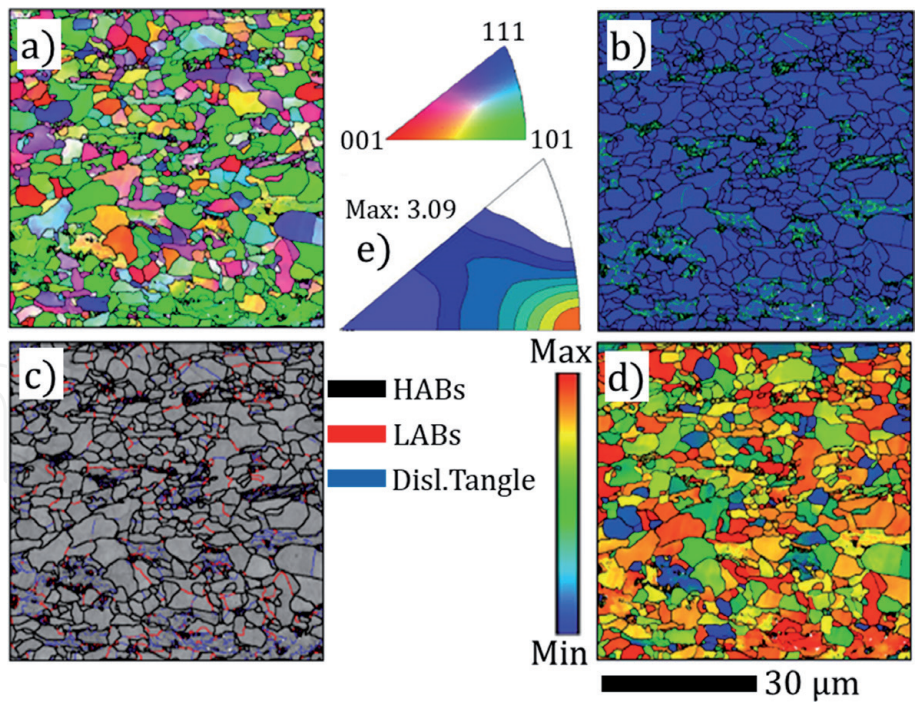
Figure 6.
(a) OI map, (b) KAM map, (c) GB map, (d) TF maps, and (e) normal direction IPF maps of the rolling plane of AIR-steel.

boundary energy is attributed by the interfacial region geometry between two adjacent crystals with different orientations. For example, the high angle boundaries (HABs), greater than 15°, are determined by point-to-point misorientation analysis [42, 43]. Low angle boundaries (LABs) and dislocation tangles were characterized from their misorientation angle (5–15° and 2–5°, respectively), **Figures 6c** and **7c**. Also, coincident site lattice (CSL) boundaries with HABs with low stored energy due to good atomic fit between neighboring crystals can act as crack arrester.
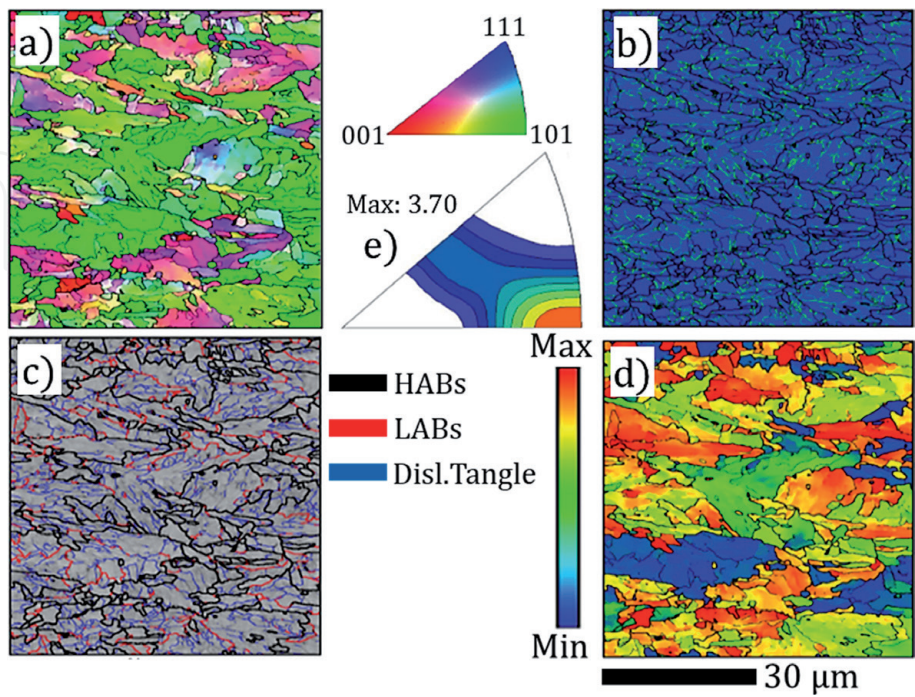
Figure 7.
(a) OI map, (b) KAM map, (c) GB map, (d) TF maps, and (e) normal direction IPF maps of the rolling plane of ACC-steel.

KAM map indicates the local plastic strain variations measured between the central point and its nearest neighbors when the misorientation between them exceeds 5° in eliminating the effect of grain boundaries [44, 45]. The high KAM angles appear cumulative build-up of misorientation inside the grain or the presence of sub-grain boundaries, **Figures 6b** and **7b**.

Pencil glide occurs on {110}, {112}, {123} slip planes along the slip direction <111>, in BCC materials such as steel. The external stress imposes during deformation leads to activate the potential activated slip systems for each grain individually according to the crystal rotation axis method based on their Schmid factors [46–48]. Polycrystalline deformation is determined through all possible combinations of the potential slip systems compared with the imposed macroscopic stress state. Then, the yield response of individual grain is predicted based on favorably and unfavorably oriented for easier slip activation according to the geometrical lattice rotation axes. For instance, soft grains with low Taylor factor value (in blue color) have the least resistance to slip, while red-colored grains represent hard grains with highest Taylor factor, i.e., highest resistance to slip [46, 47], **Figures 6d** and **7d**. Also, the corresponding rolling direction IPF obtained from each EBSD data is shown in **Figures 6e** and **7e**, which can quantify the volume fraction of the crystallographic orientation of the grains.

3.4 Tensile tests

Elongation measured at tensile tests superior to 10% and yield strength above 400 MPa for all the evaluated conditions were found. Yield strength (YS) and ultimate tensile strength (UTS) are summarized in **Figure 8**, according to the tested temperature. As shown in **Figure 8a** and considering the results at room temperature, the ACC-steel fulfills the API standard requirement for the minimum yield strength (555 MPa) [28], in the rolling and transverse planes, to be classified as X80. The AIR-steel reaches the X80 grade specification requirement in the transverse plane, but not in the rolling plane, in which it reaches only the X70 specification requirement. Considering the ultimate tensile strength at room temperature (25°C), as shown in **Figure 8b**, both plates of steel fit into the X80 grade requirement.

Regarding the results presented in **Figure 8**, it is possible to state that anisotropy was found in both plates of steel, being more intense in the AIR-steel than in the ACC-steel, which presented a smaller difference in tensile results between the rolling and transverse planes. In addition, the AIR-steel tensile test results varied considerably between temperatures due to the heterogeneity of the microstructure.

AIR-steel fails the API X80 criterion for yield stress. The ACC-steel plates were machined from a pipe, a finished product, while AIR-steel plates came directly from TMCP plate production. For AIR-steel, a further U-O-E process would be necessary to transform plates into tubes, which would promote enough work-hardening to reach the yield stress of X80-grade specification [24]. Also, the YS/UTS ratio was not the predominant factor affecting the fracture toughness, where usually high YS/UTS ratios lead to low toughness, however, in this study high YS/UTS lead to high toughness.

### 3.5 Fracture toughness tests

Fracture toughness results, measured by the CTOD parameter in mm, are summarized in **Figure 9**. For 7-mm-thick samples, AIR-steel presented lower average CTOD than ACC-steel, as shown in **Figure 9a**. AIR-steel presented difference of CTOD value between L-T and T-L geometries: L-T presented higher values than T-L. ACC-steel presented statistically equal results for both L-T and T-L. Therefore, ACC-steel presented higher toughness and less crystallographic texture effect than AIR-steel.

For 15-mm-thick samples, both steels presented a CTOD decreasing trend lowering temperatures, as depicted in **Figure 9b**. The ACC-steel depicted a better toughness behavior at 0 and −20°C than AIR-steel; however, at −40°C, both steels showed similar CTOD. CTOD results obtained at 0°C were similar to those from 7-mm-thick samples at 25°C. Below 0°C, the drop in temperature caused a partial shift of biaxial tension state towards triaxial tension state, increasing the triaxiality state at the crack-tip and reducing the material ductility [23].

To analyze the fracture surfaces, samples were submerged in liquid nitrogen and then broken by impact to separate samples into two halves. Thus, fracture surfaces of 7-mm-thick samples in **Figures 10** and 15-mm-thick samples in **Figure 11** can be observed. Fatigue pre-cracking region, crack propagation region during the CTOD test and final fracture caused by impact are also shown. The crack opening displacement (COD) and the applied force figure has been added to show the behavior of the material during the CTOD test.

For 15-mm thick samples, the AIR-steel and ACC-steel specimens were tested in L-T and T-L geometries, respectively, due to the best CTOD results of 7-mm thick samples. For AIR-steel CTOD samples, all cases tested at −20 and −40°C presented delamination during CTOD test, totalizing 6 cases. Samples tested at 0°C presented no delamination occurrence. Most of the occurred delaminations manifested as pop-ins in the CTOD test curves and four cases the delamination were considered
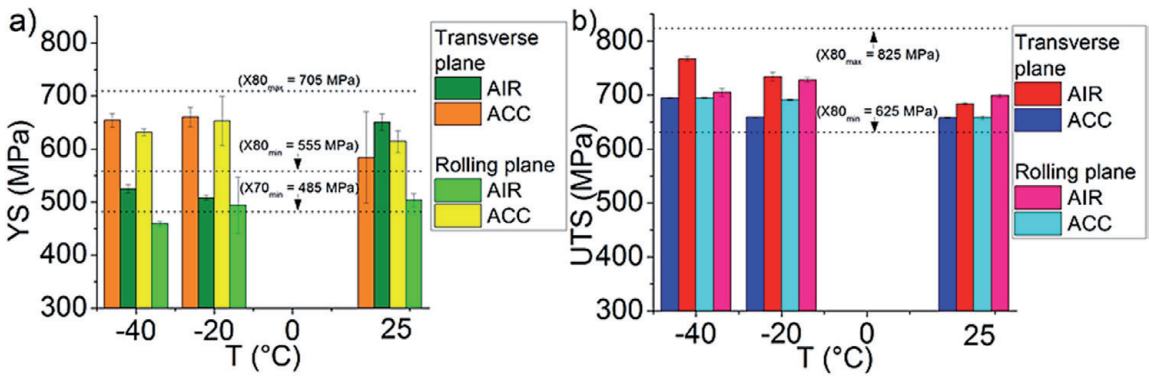
Figure 8.
Summary of the tensile tests results of the AIR-steel and ACC-steel: (a) yield strength (YS) and (b) ultimate strength (UTS). Tests were conducted in the transverse and parallel directions relative to the rolling direction.
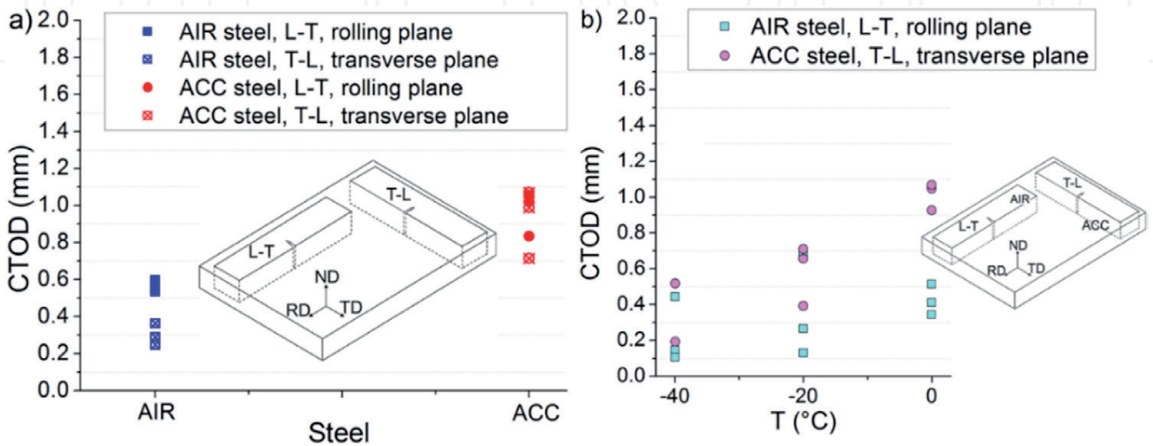
Figure 9.
Fracture toughness using CTOD parameter for ACC-steel and AIR-steel: (a) 7-mm-thick samples tested at 25°C; (b) 15-mm-thick samples tested at 0, −20 and −40°C. The L-T and T-L correspond to the ASTM E1823 [30] notches nomenclature. Tests were performed in the L-T and T-L direction in SE(B) samples. Results from ACC-steel with 15-mm-thick were published at [31].
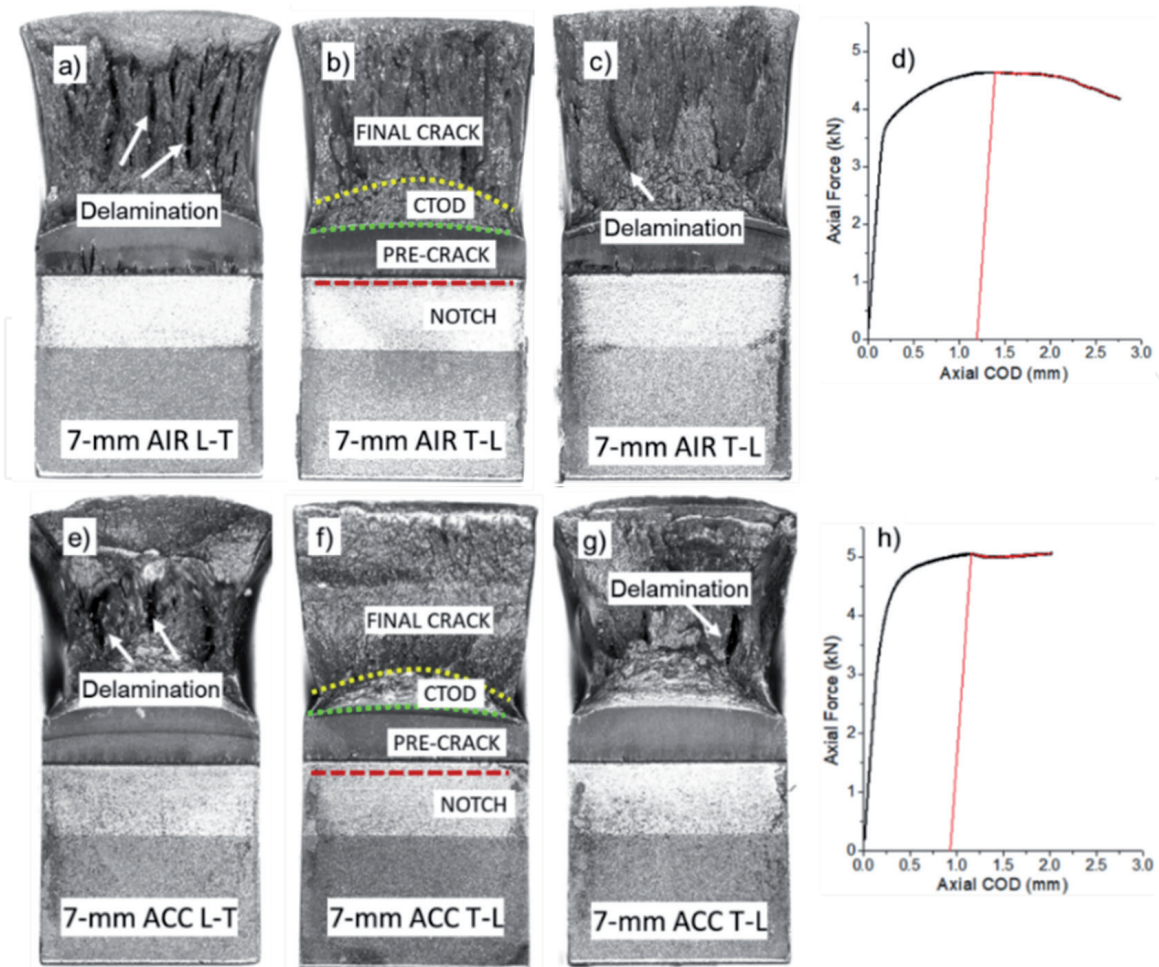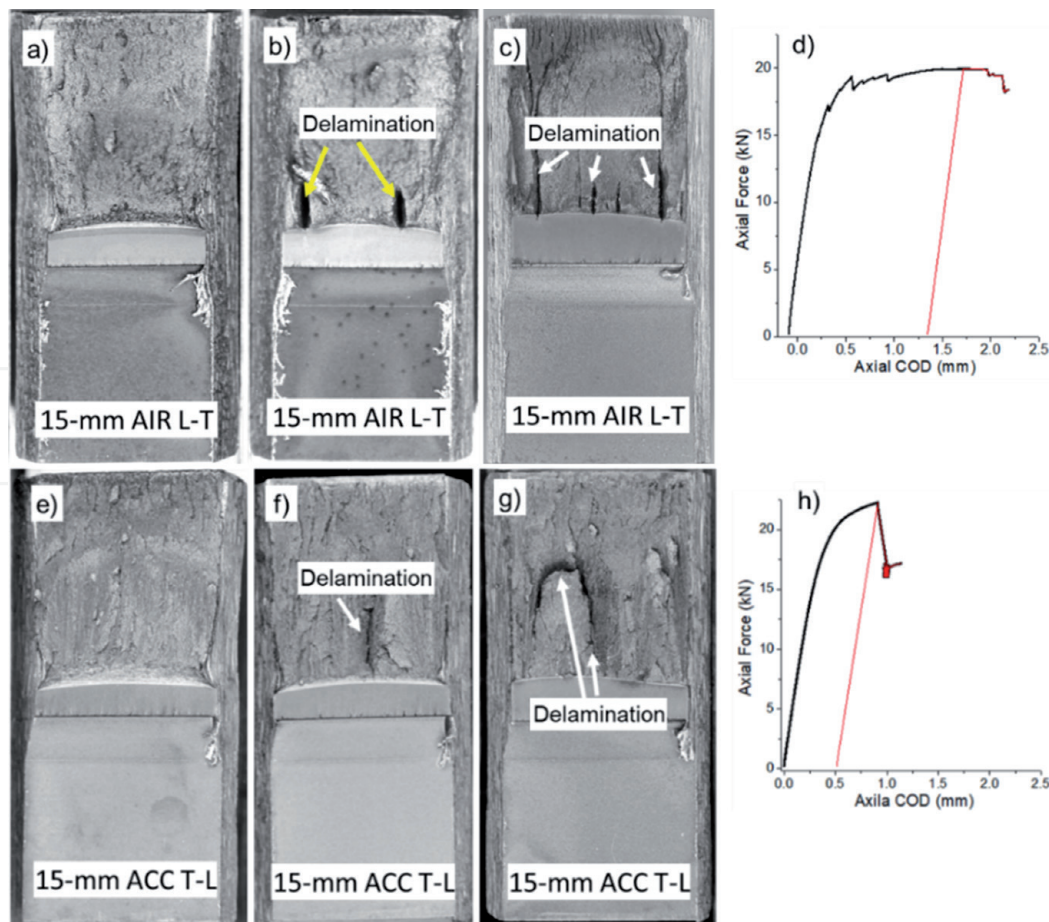
Figure 10.
Fractured surfaces of the toughness of 7-mm thick samples tested at room temperature. AIR-steel: (a) L-T geometry, plastic behavior and occurrence of delamination during sample break; (b) T-L geometry, plastic behavior on CTOD zone and flat and brittle like behavior during sample break; (c) T-L geometry, occurrence of delamination during sample break; (d) force vs. COD experimental graph during CTOD test of the sample shown in (c), displaying red line at maximum achieved force. ACC-steel: (e) L-T geometry, plastic behavior and occurrence of delamination during sample break; (f) T-L geometry, plastic behavior on CTOD zone and flat and brittle like behavior during sample break; (g) T-L geometry, plastic behavior during CTOD and final fracture, with occurrence of delamination during sample break; (h) force vs. COD experimental graph during CTOD test of the sample shown in (g), displaying red line at maximum achieved force. COD: crack open displacement at the crack mouth.

significant according to the ASTM 1820 standard [29], two at −20°C and the other two at −40°C, out of a total of 6 cases of delaminations. Notice that a pop-in event does not mean the start of brittle crack propagation, it is just a disparity of the stable crack propagation and is recommended to calculate CTOD values when they appear; however, the crack propagation continues stably until the end of the test.

Moreover, when the crack front suffers delamination, it is divided into several fronts with specific stress state in each one. Each condition is not considered in the equations to calculate CTOD by the ASTM 1820 standard [29]. This observation was previously reported by [24].

For 7-mm-thick samples, all L-T samples presented a plastic fracture aspect, with lateral deformation and a large crack propagation region during CTOD, with no delaminations, but rather after the CTOD test, during sample break, as shown in **Figure 10a**, **e**. For T-L configuration, the surface fracture presented less plastic deformation aspect in comparison to L-T, with a flatter surface. The CTOD tests did not present any abrupt drop in force, but due to high plasticity, only a gradual drop of force was presented on CTOD graphic, as depicted in **Figure 10d**, **h**.

Figure 11.
Fractured surface of API X80 15-mm thick samples tested at different temperatures. AIR-steel in L-T geometry:
(a) 0°C, plastic behavior only in CTOD zone, and no occurrence of delamination during CTOD; (b) −20°C,
low plastic behavior in CTOD zone and next to delaminations. Delaminations occurred during CTOD test,
causing pop-in; (c) brittle behavior with the occurrence of delamination during CTOD test; (d) force vs. COD
experimental graph during CTOD test of the sample shown in (c), displaying early delaminations but not
significant to end the test, and a red line at maximum achieved force. ACC-steel in T-L geometry: (e) 0°C,
plastic behavior in CTOD zone; (f) low plastic behavior in CTOD zone and occurrence of delamination
during CTOD test; (g) −40°C, brittle behavior during CTOD and final fracture, with occurrence of
delamination during CTOD; (h) force vs. COD experimental graph during CTOD test of the sample shown in
(g), displaying red line at occurred delamination, ending the test.

For ACC-steel, 4 cases tested at −20 and −40°C presented delamination during CTOD test. Samples tested at 0°C presented no delamination occurrence. All the occurred delaminations in ACC-steel were considered significant according to the ASTM 1820 standard, two at −20°C and two at −40°C.

Some fracture surfaces of 15-mm samples are presented in **Figure 11**. In general, all delaminations occurred in AIR-steel that was not considered to be significant, presented a high zone of plastic deformation near it, as in **Figure 11b**. Strain hardening is followed by pop-ins in CTOD curve, presenting a drop on CTOD force with subsequent increase of force.

4. Discussion

This study presents two TMCP X80 plates of steel with different characteristics to assess fracture of toughness and mechanisms of crack propagation and delamination of the steels. Microstructural features, such as precipitates, phase boundaries, and grain boundaries, play an important role in determining the crack

propagation by offering a weak path ahead of the crack tip. However, phase or grain boundaries can act as strong crack arrester when a crack propagates across grain boundary. Crack propagation rate inside a single-crystal grain is slower compared with the crack propagation rate along a crystal grain boundary. **Figure 12** shows the frequency of dislocation tangle, LABs, HABs and CSL for both steels in order to evaluate the capacity to offer resistance to a crack. The fraction of HABs in all planes of AIR-steel sample is greater than ACC-steel. This behavior could be attributed to the banded microstructure, secondary phases, and segregation, which produces more grain boundaries by the presence of more phases and constituents. The presence of sub-grain boundaries or LABs has indicated the arrangement of dislocation inside a single-crystal grain, retarding the crack growth. The portion of sub-grain boundaries is higher in ACC-steel, decreasing the crack propagation rate by retarding the movement of dislocation. A higher fraction of dislocation tangles of ACC-steel could be related to the more lattice distortion due to bainitic transformation without diffusion and insufficient dynamic recovery, which also decreases crack propagation rate inside a single-crystal grain. Morales-Rivas et al. reported that $\{211\}_\alpha$ habit plane identified in bainitic structure act as a barrier to the dislocation motion inside bainitic ferrite, consequently postponing the crack initiation process [49]. Although low energy CSL boundaries can effectively increase the fracture resistance and block crack propagation, no significant variation of its fraction was observed in investigated samples.

The frequency distribution of main crystallographic orientations such as {001}, {101}, and {111} with about 15° deviation from ideal planes were calculated from EBSD data of AIR and ACC-steel samples and presented in **Figure 13**. The {111} and {101} planes were predominant in the transversal and rolling planes, respectively, of the AIR-steel sample with banded ferritic microstructure with the presence of iron carbide of its structure. The {001} family of planes were found in similar proportion among the rolling and normal planes. The {001}//ND textural components were dominant on a normal plane, and {111}//ND and {101}//ND were characterized by transversal and rolling planes, respectively, in ACC-steel with bainitic structure. Such orientation-dependent mechanical properties are largely attributed to texture and crystallographic orientation, causing anisotropy of mechanical properties. It is well understood that the formation of grains lying parallel to compact planes in BCC-ferritic steel with low carbon content such as {110} and {112} enhance ductile fracture by enhancing dislocation movements by adequate activated slip system, while cleavage occurs in non-compact planes such as {001} [40, 42, 43, 50]. It is
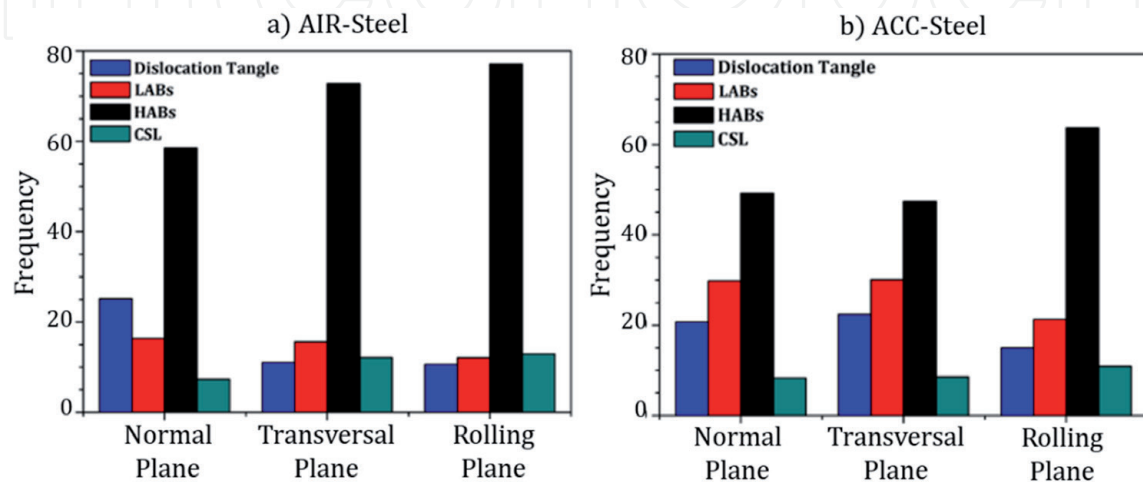
Figure 12.
Distribution of boundary types of both steels: (a) AIR and (b) ACC steel.
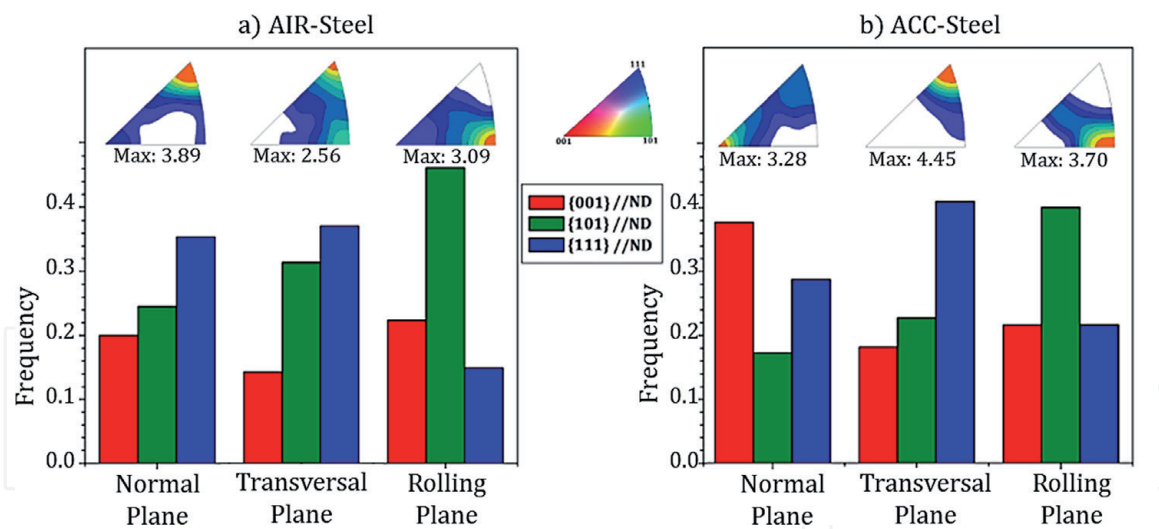
Figure 13.
Frequency distribution of main crystallographic orientations of (a) AIR-steel and (b) ACC-steel.

suggested that cleavage fracture in AIR-steel found to be influenced by banded ferrite-pearlite microstructure and formation of segregation zone. The rapid cooling at the surface allowed the formation of finer bainite orientated towards {001}//ND. Blondé et al. have been discovered that low carbon content austenite grains transform first to martensite/bainite under accelerating cooling. Das Bakshi et al. [5] investigated the Charpy impact toughness of bainitic structure of microalloyed API X70 steels. They also characterized a dominance of a large fraction of {111}//ND grains accompanied by the presence of {001} and {101} because of the less of recrystallized austenite before the bainitic transformation of austenitic grains. However, this bainitic structure has less distortion rather than martensite structure, thereby, exhibited less risk of cleavage fracture.

KAM values indirectly measure the dislocation density and the local plastic strain developed in the steel during rolling processing and were presented in **Figures 6** and **7**. The presence of banded ferrite—pearlite microstructure with the dispersion of secondary particles induced local stress sites concentration that would make AIR-steel sample prone to crack initiation due to the local high elastic energy stored. Inhomogeneous dislocation accumulation at interfaces traps carbon atoms, resulting in brittle carbide precipitates containing high dislocation density, leading to early fracture. It is included that the dislocation piles up concentrated at ferrite grain boundaries increase the risk of microcrack nucleation and crack propagation as well. However, the bainitic packet containing strain localization inside the soft ferrite lath phase decreases the strain gradient between the inside and at boundary region [51], resulting in higher strain hardenability and more fracture resistance.

Full constraint Taylor approach was used to evaluate the potential activated slip systems dependent on the grain orientations (**Figures 6** and **7**). It is found that the AIR-steels had a more distribution of high Taylor factor in comparison with ACC-steel, indicating the higher capability of storage of energy due to the accumulation of larger dislocation densities or dislocation piles-up, due to more active slip systems in a certain direction. ACC-steel with low Taylor Factor bainitic structure limits the deformation ability by not offering adequate slip systems. These assessments agree with the tensile results obtained in **Figure 8** where AIR-steel presented a higher UTS/YS relation in comparison to ACC-steel.

AIR-steel presented higher intensity on {001} <110> to {111} <110> alpha-fiber, and {111} <110> to {111} <112> gamma-fiber than ACC-steel because of a lower finishing rolling temperature. AIR-steel presented stronger {100} <011>, known as rotated

cube texture, than ACC-steel, which possess a low Taylor factor, i.e., high strain stored energy, or low further deformation ability. This result indicates intense cold deformation, low finish rolling temperature and low inter-pass rolling time [52, 53].

This non-random distribution of crystal orientations influenced toughness properties, mainly by triggering delamination phenomena. The occurrence of delamination for 7-mm thick samples only occurred out of CTOD zone, after test, during sample break. For 15-mm thick sample, delaminations occurred during CTOD tests, causing pop-in and instant drop on the force.

Crystallographic orientation has been reported to be the major role causing impact toughness anisotropy of the steels [5, 8, 10, 17, 23, 54]. Some atomic planes are more important, as {110}, {112} and {123}, which are the major slip system for BCC steels [5, 8], and the {100}, which is the cleavage plane, the cube side lattice, for BCC steels [5, 8, 10, 17, 23, 54]. Also, it is important to bear in mind that the effect of these planes upon mechanical properties will depend on the volume, distribution and mainly on the position relative to the applied forces and planes presented during crack propagation at the crack-tip. For instance, for cleavage to occur, plane {100} must be presented perpendicular to the applied force, i.e., parallel to the fracture plane. To trigger the {112} slip system, the plane must be placed parallel to the applied force, i.e., perpendicular to the fracture plane.

The alpha-fiber is a parallel fiber to the RD and presents some of the planes mentioned above as {100}, {112} and {113}. It was reported that the sharpening the {112} <110> and {113} <110> components results in improvement of impact toughness [5, 8, 25, 54]. As shown in **Figure 5f**, AIR-steel has a peak intensity at {001} <110>, followed by a dip and then peak at ϕ = 20–30°, region of {112} and {113} components. ACC-steel presents a plateau between ϕ = 10–35°. Values of intensity are higher for AIR-steel than for ACC-steel. Nonetheless, ACC-steel presented higher CTOD toughness with better isotropy, while AIR-steel presented lower values and anisotropy according to the geometry sample. These results are consistent with another study [8] in which was reported a higher fraction of {112} <110> at L-T than T-L and yet much higher CTOD results were obtained with T-L than L-T, showing no specific correlation of increasing toughness by increasing {112}.

The obtained results show slight crystallographic differences between L-T and T-L configurations, and, for ACC-steel, these differences did not seem to affect toughness. However, it is suggested that the anisotropy displayed by AIR-steel between L-T and T-L geometries relies not only crystallographic orientation discrepancies but the microstructure anisotropy, as also reported [27]. 7-mm AIR-steel presented a higher fracture toughness for L-T configuration than T-L, in which the crack travels on a parallel plane to the rolling plane. Comparing L-T to T-L configurations of AIR-steel, nothing between is different regarding the chemical composition of phases and constituents, but only regarding the distribution and configuration of the microstructure.

For AIR-steel, there is anisotropy of grain morphology and segregation configuration, as depicted schematically in **Figure 14**. Segregation is present on both geometries, but its configuration is different in each case, as for L-T geometry, segregation is transverse to the rolling plane while for T-L, segregation is coincident to the rolling plane as shown in **Figure 14**. Banded regions and the presence of aligned microphases and non-metallic inclusions, such as MnS, create an easy path for crack propagation, influencing toughness according to their volume, morphology and distribution [5, 15]. Ferrite resists the crack propagation better than bands composed of secondary phases and constituents, which act as brittle sites for crack initiation or as a concentrated stress spot, an easy path for the crack propagation [22]. For AIR-steel 7-mm L-T geometry, the fine equiaxed grain is encountered, while for T-L geometry, elongated rolled grains are found. Grain morphology of

7-mm ACC-steel was similar in the transverse and rolling planes, the tensile and toughness values were also similar in both directions.

For 15-mm thick samples, a general decrease is observed with a reduction of temperature. An approximate DBTT is −20°C, once, at this temperature, the values of toughness resulted from CTOD tests were close to a mean value of 0°C with −40°C condition tests. Overall, AIR-steel presented lower toughness than ACC-steel. As the temperature was lowered, the fracture started to present a more brittle-like behavior — this induced delamination occurrence, as well as a dropping tendency on toughness. Many 15-mm thick samples presented delaminations, and all delaminations were of divider type, as shown in **Figure 15**.

For all delaminations not considered significant, posterior plastic deformation and strain-hardening are achieved, increasing the CTOD force during test. These delaminations happen because the divider delamination branches the crack into two or more crack fronts, causing a relaxation of the triaxial tension towards a state of biaxial tension resulting in the decrease of the overall material constraint, promoting strain-hardening [22, 23]. In the cases of significant delamination, little or no
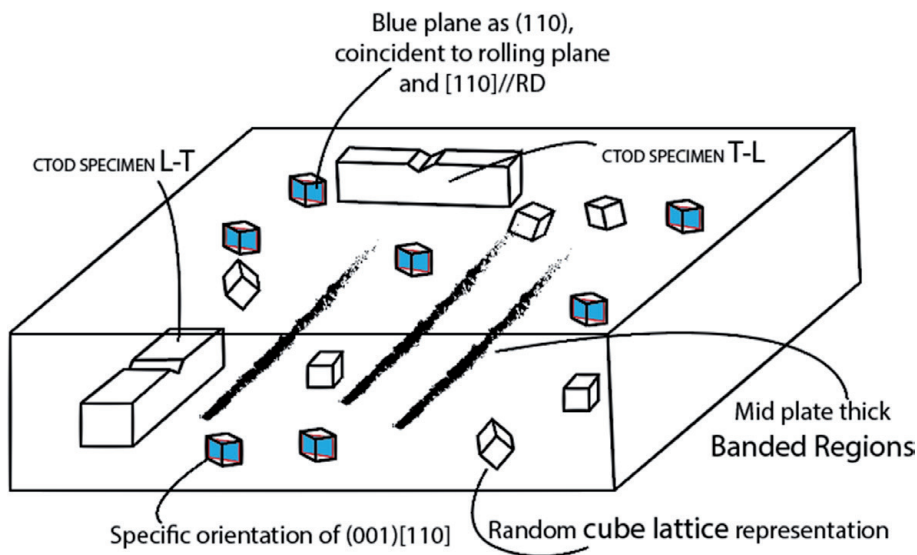
Figure 14.
Schematic illustration of the used AIR-steel. CTOD specimens in L-T and T-L configuration shown to better visualize the relationship between the microstructure on the CTOD crack propagation path and global plate microstructure.
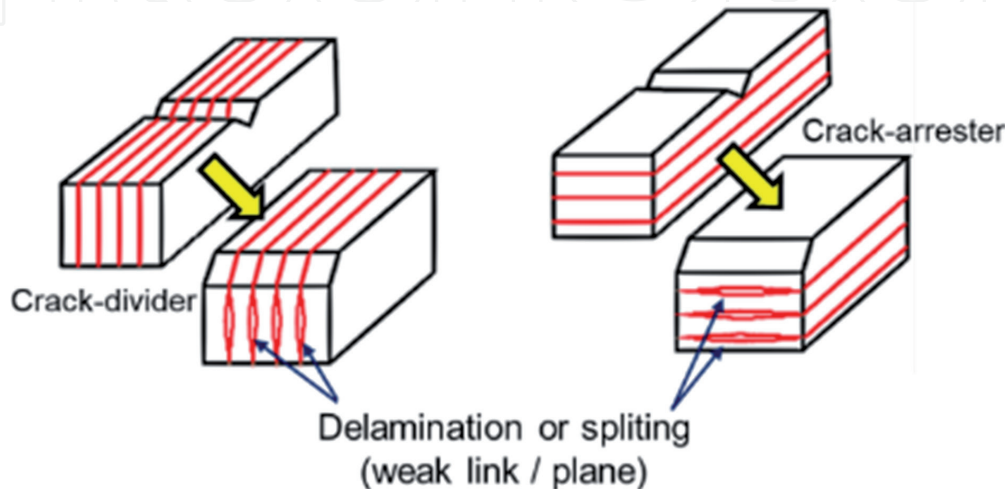
Figure 15.
Delamination morphology: divide or arrester.
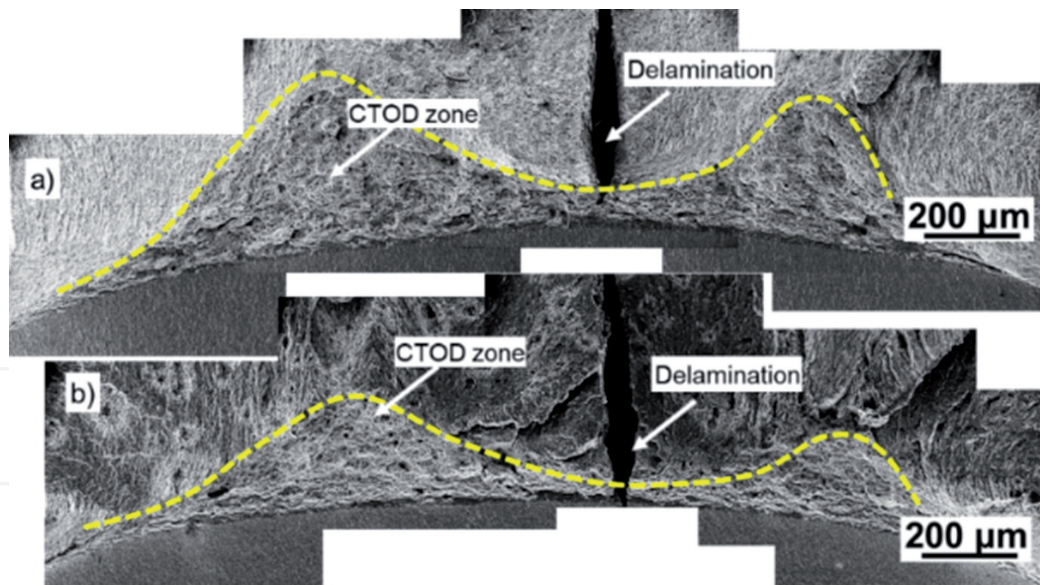
Figure 16.
CTOD fracture surface of API X80 AIR-steel samples tested at different temperatures. Condition tested at (a) 25°C, showing a more plastic extension of CTOD zone, and plastic deformation on delamination edges; (b) −40°C, still exhibiting a plastic character in CTOD zone, but for a shorter extension. Yellow pointed line representing CTOD zone delimitation.

strain-hardening ability was promoted. **Figure 16** shows a fracture surface with non-significant and significant delamination, showing an aspect more plastic in the former case.

Many works studied the cause of delamination, assigning it to the presence of {100} cleavage plane [5, 8, 10, 23], but without further explanations. Some authors believe that delaminations are consequence mostly of the microstructure [26, 27]. In fact, microstructure exerts an effect on delamination occurrence, since AIR-steel presented more cases of delamination than ACC-steel, but not playing a major role. ACC-steel presented delamination on CTOD for 15-mm and on sample breaking for 7-mm, and yet presented a homogeneous microstructure with no detected inclusions or oxides, and not presenting mid-thickness segregation as AIR-steel.

Delamination phenomena are mainly governed by the crystallographic orientation presented next to the crack propagation path. It is necessary to fulfill embrittlement factors to satisfy the delamination criterion, i.e., many related parameters as temperature, crystallographic planes and orientations and presence of brittle phases. Regarding crystallographic orientation, the many previous works cited above correlated all delamination cases to the presence of {001}.

The X-ray diffraction results showed low presence of {001} parallel to fracture plane in L-T and T-L geometries, and intense {001} at 45° to fracture plane. **Figure 17** shows exactly the display of alpha-fiber according to L-T configuration. The delamination takes place traveling the {001} cubes face, macroscopically display at 45° to the fracture plane.

Figure 18 illustrates the CTOD sample and the path of crack propagation, containing grains with random crystallographic orientations. The red-colored cube representing the {100} <011>, and the presence a possible clustering of {100} <011>. If two adjacent grains possess the same orientation, then they belong to the same grain. Therefore, it is assumed the existence of slight misorientation between schematic cubes. During the CTOD test, an external force produces internal stresses, causing transmission of forces in each atom lattice. This force transmission assuming the cubic lattice reaches a maximum shear component exactly when the vertex of the cube is pointing out to the applied force. In other words, a maximum shear in the lattice is achieved when the plane <011> is parallel to the applied force.
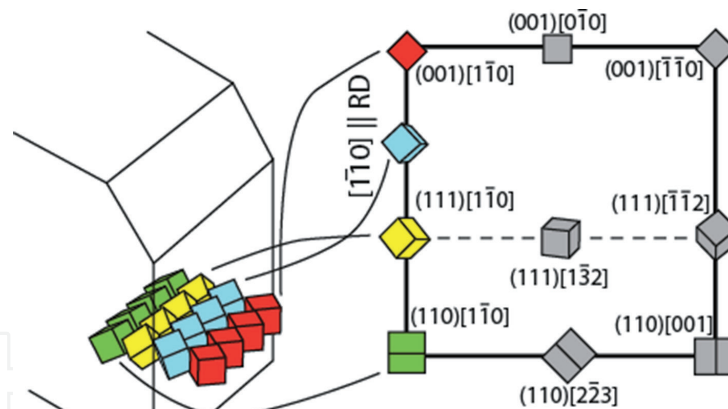
Figure 17.
Schematic illustration containing half of SE(B) CTOD samples and crystallographic representation on fracture plane with alpha-fiber for L-T configuration.
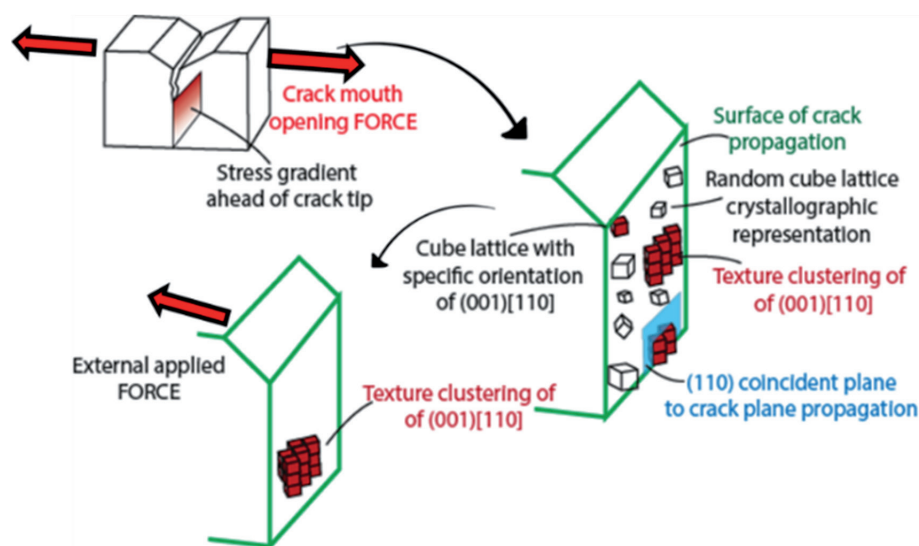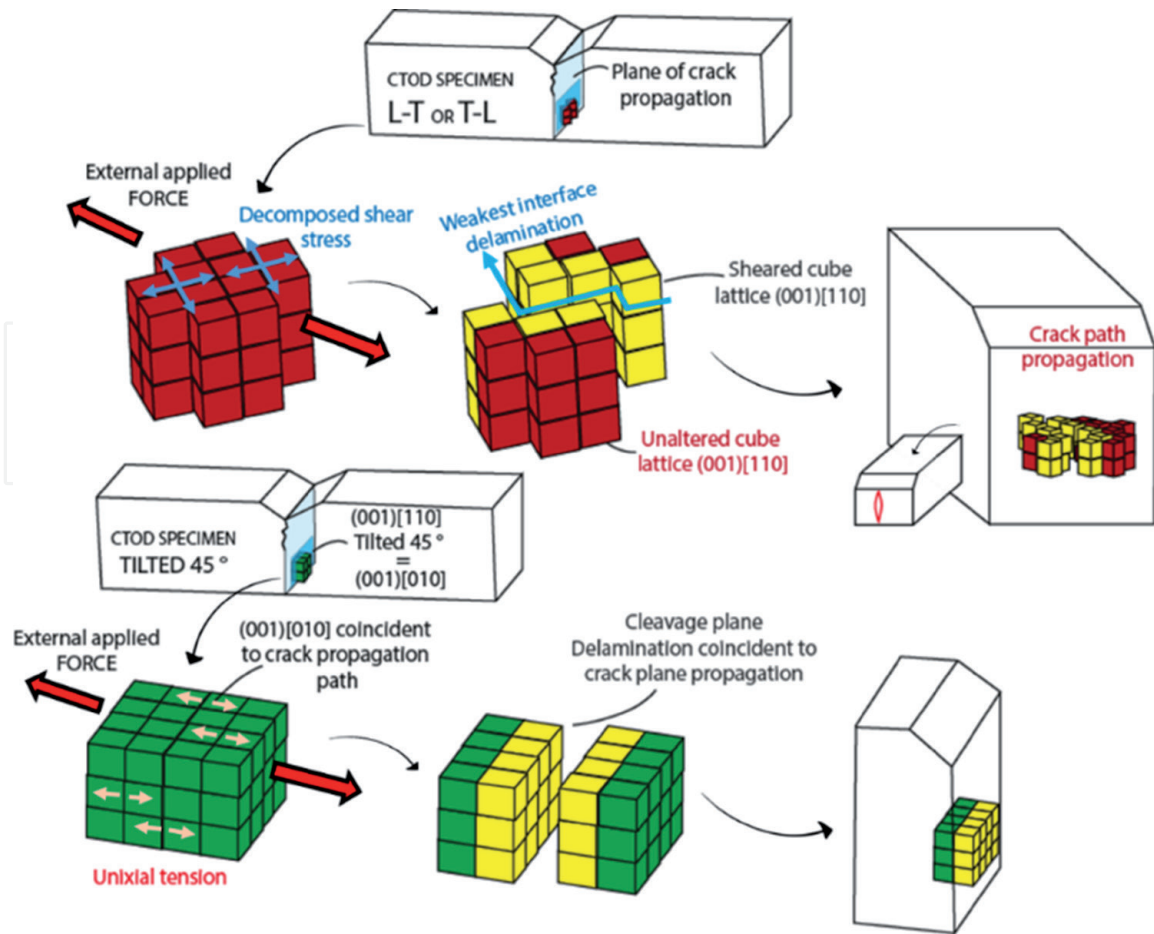

Figure 18.
Schematic illustration of CTOD sample and the crystallographic orientations contained by the fracture plane. To a given a textured sample with high alpha-fiber, the first component is (001)[110] of the system {100} <011>, will present high intensity, existing the possibility of very similar oriented grains to be close to each other, forming a cluster.

That is exactly the role of the {100} <011> in delaminations occurrence. Applying a 45° rotation, the face of the cube coincides the imaginary plane of fracture. In this configuration, when an external force is applied, there is no shear component but only uniaxial tension directly on the cleavage plane {100}. Thus, plastic deformation is suppressed, lowering any mechanical property measured.

The literature agrees with the proposed model of **Figure 19**. Mouriño et al. reported the lowest impact toughness at 45° from the RD. This result can be attributed to the highest volume fraction of {001} cleavage planes parallel to the 45° to the RD macroscopic fracture plane [54].

Yang et al. presented three different rolled and heat-treated conditions for the same chemical composition and no macrosegregation. The final difference was grain morphology (elongated for the cold-worked) and texture. Results reported showed the lowest impact toughness and presence of delamination for the elongated grain morphology and the highest fraction of {100} on the fracture plane [25]. Joo et al. reported similar results, the lowest toughness at 45° with a high fraction of {100} planes [10]. In this study, samples were machined from the same rolled and treated plate, excluding any microstructure influence. It

Figure 19.
Schematic illustration of CTOD sample in L-T, T-L configurations, and tilted 45° from RD. Explaining how delamination occurs, and why the 45° tilted sample presents the worst toughness according to the literature.

was concluded that the dominant aspect of anisotropy was the crystallographic texture. Furthermore, the anisotropy was enhanced when a near DBTT temperature was used [10]. These cited results are very similar to the obtained result in the present paper.

The microstructure may have affected the delamination occurrence, once AIR-steel presented more delaminations than ACC-steel and showed a macrosegregation in the mid-thickness of the plate and elongated grains. It is also important to highlight that the observed delaminations occurred not only next to the mid-thickness of the samples, showing that microstructure banding is not the major or unique factor to trigger delamination. As expected, testing samples in RD or TD showed little difference for a homogeneous microstructure. Changing from RD to TD results only in slight crystallographic difference for a cubic system. AIR-steel presented a decrease of toughness mainly due to the change of polygonal to elongated microstructure.

Toughness value is mainly controlled by crystallographic feature, and delaminations have a straight relation to the presence of {100} specifically on the plane of fracture [5, 8, 9, 10, 17, 23, 25, 54]. The alpha-fiber plays an important role because it aligns the [110] direction to RD, as shown in **Figure 17**, and, usually, the rolling process produces strong alpha-fiber, therefore, strong (100)[011]. This condition leads to a strong (100)[010] at 45° from RD, resulting in the lowest toughness as reported [10, 25, 54], and it is in agreement with the present work and proposed model in **Figure 19**. However, the 45° to RD configuration is not the cause of low toughness, but the presence of {100} on the fracture plane. Bakshi et al. obtained high toughness at 45° and low toughness at RD and ND (0 and 90° to RD) due to low {100} at 45° to RD [5].

5. Conclusions

- Delamination is governed by the presence of a specific crystallographic orientation. For the present work and others cited from literature, the {100} <011> is the main orientation that triggers delamination.

- This work presented a schematic model of how the presence of {100} on fracture plane causes cleavage. The acting forces became nearly maximum uniaxial as Mohr theory, suppressing plastic deformation and cleavage fracturing.

- The presented model clarifies the reason for generally rolled plates presenting lowest toughness at 45° to RD. Furthermore, the strong alpha-fiber is translated to strong {100} 45° to RD according to a cubic lattice system, causing cleavage through {100} coincident to the fracture plane.

- The texture is the main factor causing anisotropy that affects toughness.

- Macrosegregation and grain morphology affects the toughness of steel. As similar crystallography is obtained//RD and //ND for a cubic lattice, ACC-steel did not present toughness change for L-T and T-L configuration, while AIR-steel presented lower toughness on the elongated grain plane T-L.

- ACC-steel and AIR-steel plates were produced by TMCP, with accelerated-cooling and air-cooling in the final production stage, respectively. Moreover, both steels presented differences in mechanical properties and fracture toughness due to anisotropy and heterogeneities in the microstructure. ACC-steel exhibited a granular bainitic microstructure, which increased hardness and fracture toughness compared to AIR-steel.

Acknowledgements

Author details

Fabio Faria Conde[1], Haroldo Cavalcanti Pinto[1], Mohammad Masoumi[2] and Julian Arnaldo Avila[3*]

1 USP – University of São Paulo, SP, Brazil

2 Center for Engineering, Modeling and Applied Social Sciences (CECS), Universidade Federal do ABC (UFABC), SP, Brazil

3 UNESP – São Paulo State University (UNESP), SP, Brazil

*Address all correspondence to: julian.avila@unesp.br

IntechOpen

References

[1] Bai Y, Bai Q, editors. Subsea Engineering Handbook. Gulf Professional Publishing; 2010. pp. 919. ISBN: 9781856176897. DOI: 10.1016/B978-1-85617-689-7.10030-5. Available from: http://www.sciencedirect.com/science/article/pii/B9781856176897100305

[2] Bai Y, Bai Q, editors. Subsea Pipelines and Risers. Elsevier Science Ltd; 2005. pp. 808. ISBN: 9780080445663. DOI: 10.1016/B978-008044566-3.50043-9. Available from: http://www.sciencedirect.com/science/article/pii/B9780080445663500439

[3] Nishioka K, Ichikawa K. Progress in thermomechanical control of steel plates and their commercialization. Science and Technology of Advanced Materials. 2012;**13**(2):023001

[4] Militzer M. 1.10 - Thermomechanical Processed Steels. In: Saleem H, Gilmar FB, Chester JVT, Bekir Y, editos. Comprehensive Materials Processing. Elsevier; 2014. pp. 191-216. ISBN: 9780080965338. DOI: 10.1016/B978-0-08-096532-1.00115-1. Available from: http://www.sciencedirect.com/science/article/pii/B9780080965321001151

[5] Das Bakshi S, Dhande T, Javed N, Sasidhar KN, Sharma V, Mukherjee M, et al. Effect of hot deformation and crystallographic texture on toughness anisotropy and fracture behavior of Nb+V microalloyed API X70 steel. International Journal of Pressure Vessels and Piping. 2019;**171**:162-172. Available from: https://linkinghub.elsevier.com/retrieve/pii/S0308016118302217

[6] Sung HK, Lee S, Shin SY. Effects of start and finish cooling temperatures on microstructure and mechanical properties of low-carbon high-strength and low-yield ratio bainitic steels. Metallurgical and Materials Transactions A, Physical Metallurgy and Materials Science. 2014;**45**(4):2004-2013

[7] Gervasyev A, Carretero Olalla V, Sidor J, Sanchez Mouriño N, Kestens LAI, Petrov RH. An approach to microstructure quantification in terms of impact properties of HSLA pipeline steels. Materials Science and Engineering A. 2016;**677**:163-170

[8] Chatterjee S, Koley S, Das Bakshi S, Shome M. Role of crystallographic texture, delamination and constraint on anisotropy in fracture toughness of API X70 line pipe steels. Materials Science and Engineering A. 2017;**708**:254-266. DOI: 10.1016/j.msea.2017.09.104

[9] Joo MS, Suh DW–W, Bae JH, Bhadeshia HKDH. Role of delamination and crystallography on anisotropy of Charpy toughness in API-X80 steel. Materials Science and Engineering A. 2012;**546**:314-322. DOI: 10.1016/j.msea.2012.03.079

[10] Joo MS, Suh DW, Bae JH, Sanchez Mouriño N, Petrov R, Kestens LAI, et al. Experiments to separate the effect of texture on anisotropy of pipeline steel. Materials Science and Engineering A. 2012;**556**:601-606

[11] Joo MS, Suh DW, Bhadeshia HKDH. Mechanical anisotropy in steels for pipelines. ISIJ International. 2013;**53**(8):1305-1314. Available from: http://jlc.jst.go.jp/DN/JST.JSTAGE/isijinternational/53.1305?lang=en&from=CrossRef&type=abstract

[12] Mintz B, Morrison WB, Morris PP, Davies GJ. The influence of texture on the tensile and impact properties of controlled steels. In: Davies GJ, editor. Texture and Properties of Materials. London, UK: The Metal Society; 1976. pp. 224-234

[13] Inagaki H, Kurihara K, Kozasu I. Influence of crystallographic texture on the strength and toughness of control-rolled high tensile strength steel. ISIJ International. 1977;**17**:75-81

[14] Sung HK, Sohn SS, Shin SY, Lee S, Kim NJ, Chon SH, et al. Effects of finish rolling temperature on inverse fracture occurring during drop weight tear test of API X80 pipeline steels. Materials Science and Engineering A. 2012;**541**:181-189. DOI: 10.1016/j.msea.2012.02.019

[15] Ghosh A, Modak P, Dutta R, Chakrabarti D. Effect of MnS inclusion and crystallographic texture on anisotropy in Charpy impact toughness of low carbon ferritic steel. Materials Science and Engineering A. 2016;**654**:298-308. DOI: 10.1016/j.msea.2015.12.047

[16] Ghosh A, Kundu S, Chakrabarti D. Effect of crystallographic texture on the cleavage fracture mechanism and effective grain size of ferritic steel. Scripta Materialia. 2014;**81**:8-11. DOI: 10.1016/j.scriptamat.2014.02.007

[17] Zong C, Zhu G, Mao W. Effect of crystallographic texture on the anisotropy of Charpy impact behavior in pipeline steel. Materials Science and Engineering A. 2013;**563**:1-7. DOI: 10.1016/j.msea.2012.11.055

[18] Mineur M, Villechaise P, Mendez J. Influence of the crystalline texture on the fatigue behavior of a 316L austenitic stainless steel. Materials Science and Engineering A. 2000;**286**(2):257-268

[19] Avila JA, Lucon E, Sowards J, Mei PR, Ramirez AJ. Assessment of ductile-to-brittle transition behavior of localized microstructural regions in a friction-stir welded X80 pipeline steel with miniaturized Charpy V-notch testing. Metallurgical and Materials Transactions A, Physical Metallurgy and Materials Science. 2016;**47**(6):2855-2865

[20] Lucon E. Testing of Small-Sized Specimens. In: Comprehensive Materials Processing [Internet]. Elsevier; 2014. p. 135-163. Available from: https://linkinghub.elsevier.com/retrieve/pii/B9780080965321001102

[21] Tunnicliffe MC. The Fracture Toughness of Low Carbon Steels; The Effects of Grain Size and Temperature. PhD thesis. University of Canterbury; 1991

[22] Joo MS, Suh D-W, Bhadeshia DH. Anisotropy of Charpy properties in linepipe steels. ISIJ International. 2013;**53**:1305-1314

[23] Kimura Y, Inoue T, Fuxing YIN, Tsuzaki K. Delamination toughening of ultrafine grain structure steels processed through tempforming at elevated temperatures. ISIJ International. 2010;**50**(1):152-161. Available from: http://www.scopus.com/inward/record.url?eid=2-s2.0-77949815730&partnerID=40&md5=e3206b9cc9b2a4b7ca5866e292637020

[24] Ávila JAD, Ruchert COFT, Mei PR, Reppold RM, Piza MTP, Ramirez AJ. Fracture toughness assessment at different temperatures and regions within a friction stirred API 5L X80 steel welded plates. Engineering Fracture Mechanics. 2015;**147**:176-186

[25] Yang XL, Xu YB, Tan XD, Wu D. Relationships among crystallographic texture, fracture behavior and Charpy impact toughness in API X100 pipeline steel. Materials Science and Engineering A. 2015;**641**:96-106

[26] Pyshmintsev I, Gervasyev A, Petrov RH, Carretero Olalla V, Kestens L. Crystallographic texture as a factor enabling ductile fracture arrest in high strength pipeline steel. Materials Science Forum. 2011;**702-703**:770-773. Available from: https://www.scientific.net/MSF.702-703.770

[27] Petrov RH, García OL, Mouriño NS, Kestens L, Bae JH, Kang KB. Microstructure - texture related toughness anisotropy of API-X80 pipeline steel characterized by means of 3D-EBSD technique. Materials Science Forum. 2007;**558-559**:1429-1434

[28] Specification for Line Pipe. ISO 3183:2007 (Modified). American Petroleum Institute; 2009. p. 176

[29] ASTM F1820-13. Standard Test Method for Determining the Forces for Disassembly of Modular Acetabular Devices. West Conshohocken, PA: ASTM International; 2013. www.astm.org

[30] ASTM E1823-13. Standard Terminology Relating to Fatigue and Fracture Testing. West Conshohocken, PA: ASTM International; 2013. www.astm.org

[31] Avila JA, Rodriguez J, Mei PR, Ramirez AJ. Microstructure and fracture toughness of multipass friction stir welded joints of API-5L-X80 steel plates. Materials Science and Engineering A. 2016;**673**:257-265

[32] ASTM E8 / E8M-16a. Standard Test Methods for Tension Testing of Metallic Materials. West Conshohocken, PA: ASTM International; 2016. www.astm.org

[33] Zajac S, Schwinn V, Tacke KH. Characterisation and quantification of complex bainitic microstructures in high and ultra-high strength linepipe steels. Materials Science Forum. 2005;**500-501**:387-394

[34] Cizek P. Transformation behaviour and microstructure of an API X80 linepipe steel subjected to simulated thermomechanical processing. Metal. 2001;**15**:1-8

[35] Silva RDA, Souza LFG, Morales EV, Rios PR, Bott IDS. Formation of microphases and constituents from remaining austenite decomposition in API X80 steel under different processing conditions. Materials Research. 2015;**18**(5):908-917

[36] Yan P, Bhadeshia HKDH. Mechanism and kinetics of solid-state transformation in high-temperature processed linepipe steel. Metallurgical and Materials Transactions A: Physical Metallurgy and Materials Science. 2013;**44**:5468-5477

[37] Bhadeshia HKDH, HoneycombeRWK.In:Lecomte-BeckersJ, Schubert F, Ennis PJ, editors. Steels: Microstructure and Properties. 3rd ed. Vol. 3. Oxford: Elsevier Ltd; 2006. p. 357

[38] Suwas S, Gurao NP. Crystallographic texture in Materials. Journal of the Indian Institute of Science. 2008;**88**:151-177

[39] Bunge HJ. Texture Analysis in Materials Science. Butterworth-Heinemann; 1982. pp. 593. ISBN: 9780408106429. DOI: 10.1016/B978-0-408-10642-9.50002-7. Available from: http://www.sciencedirect.com/science/article/pii/B9780408106429500027

[40] Suikkanen PP, Cayron C, Deardo AJ, Karjalainen LP, Oy RM, Box PO, et al. Crystallographic analysis of isothermally transformed bainite in 0.2C-2.0Mn-1.5Si-0.6Cr steel using EBSD. Journal of Materials Science and Technology. 2013;**29**(4):359-366

[41] Yan J, Zhang W, Borgenstam A. Observations of surface relief of proeutectoid widmansta cementite plates in a hypereutectoid carbon steel. Metallurgical and Materials Transactions A: Physical Metallurgy and Materials Science. 2013;**44**:4143-4149

[42] Masoumi M, Silva CC, Ferreira H, Abreu, De G. Effect of crystallographic orientations on the hydrogen-induced cracking resistance improvement of API 5L X70 pipeline steel under

various thermomechanical processing. Corrosion Science. 2016;**111**:121-131

[43] Mohtadi-bonab MA, Eskandari M, Sanayei M, Das S. Microstructural aspects of intergranular and transgranular crack propagation in an API X65 steel pipeline related to fatigue failure. Engineering Failure Analysis. 2018;**94**:214-225

[44] Zhang X, Matsuura K, Ohno M. Misorientation/local plastic strain manifestations in chemical etching color. Micron. 2014;**59**:28-32

[45] Chen Y, Tsai Y, Tung P, Tsai S, Chen C, Wang S. Phase quantification in low carbon Nb-Mo bearing steel by electron backscatter diffraction technique coupled with kernel average misorientation. Materials Characterization. 2018;**139**:49-58

[46] Kocks UF, Chandra H. Slip geometry in partially constrained deformation. Acta Metallurgica. 1982;**30**:695-709

[47] Zheng X, Zhang H. Experimental determination of deformation induced lattice rotation by EBSD technique for slip system analysis. Journal of Materials Science and Technology. 2017;**33**:90-98

[48] Taylor GI. Plastic Strain in Metals. Journal of the Institute of Metals. 1938;**62**:307-324

[49] Morales-rivas L, Archie F, Zaefferer S, Benito-alfonso M, Tsai S, Yang J, et al. Crystallographic examination of the interaction between texture evolution , mechanically induced martensitic transformation and twinning in nanostructured bainite. Journal of Alloys and Compounds. 2018;**752**:505-519

[50] Masoumi M, Echeverri EAA, Silva CC, Aguiar WM, de Abreu HFG. Improvement of formability and tensilemechanical properties of SAE 970X steel bycontrolled rolling process. Journal of Materials Research and Technology. 2018;**8**(1):1353-1365

[51] Ishikawa N, Yasuda K, Sueyoshi H, Endo S, Ikeda H, Morikawa T, et al. Microscopic deformation and strain hardening analysis of ferrite— Bainite dual-phase steels using micro-grid method. Acta Materialia. 2015;**97**:257-268

[52] Chang SK, Il LS, Lee DN. Change of rotated cube texture through multi-processing in 3% Si-steels. ISIJ International. 2009;**49**(1):105-108

[53] Takajo S, Vogel SC, Hayakawa Y. Strongly developed texture components near rotated cube orientation during recrystallization in a severely cold rolled low carbon steel. ISIJ International. 2019;**59**(3):541-550

[54] Mouriño NS, Petrov R, Bae JH, Kim K, Kestens LAI. Texture dependent mechanical anisotropy of X80 pipeline steel. Advanced Engineering Materials. 2010;**12**(10):973-980